
































# BlackTHUNDER strikes twice: rest-frame Balmer-line absorption and high Eddington accretion rate in a Little Red Dot at $z = 7.04$

Francesco D’Eugenio <sup>1,2\*</sup>, Roberto Maiolino <sup>1,2,3</sup>, Michele Perna <sup>4</sup>, Hannah Übler <sup>5</sup>, Xihan Ji <sup>1,2</sup>, William McClymont <sup>1,2</sup>, Sophie Koudmani <sup>1,6</sup>, Debora Sijacki <sup>1,7</sup>, Ignas Juodžbalis <sup>1,2</sup>, Jan Scholtz <sup>1,2</sup>, Jake Bennett <sup>8</sup>, Andrew J. Bunker <sup>9</sup>, Stefano Carniani <sup>10</sup>, Stéphane Charlot <sup>11</sup>, Giovanni Cresci <sup>12</sup>, Emma Curtis-Lake <sup>6</sup>, Elena Dalla Bontà <sup>13,14,15</sup>, Gareth C. Jones <sup>1,2</sup>, Jianwei Lyu <sup>16</sup>, Alessandro Marconi <sup>17,12</sup>, Giovanni Mazzolari <sup>18,19</sup>, Erica J. Nelson <sup>20</sup>, Eleonora Parlanti <sup>10,5</sup>, Brant E. Robertson <sup>21</sup>, Raffaella Schneider <sup>22</sup>, Charlotte Simmonds <sup>1,2</sup>, Sandro Tacchella <sup>1,2</sup>, Giacomo Venturi <sup>10</sup>, Chris Willott <sup>23</sup>, Joris Witstok <sup>24,25</sup> and Callum Witten <sup>26</sup>

<sup>1</sup>Kavli Institute for Cosmology, University of Cambridge, Madingley Road, Cambridge, CB3 0HA, United Kingdom

<sup>2</sup>Cavendish Laboratory - Astrophysics Group, University of Cambridge, 19 JJ Thomson Avenue, Cambridge, CB3 0HE, United Kingdom

<sup>3</sup>Department of Physics and Astronomy, University College London, Gower Street, London WC1E 6BT, UK

<sup>4</sup>Centro de Astrobiología (CAB), CSIC-INTA, Cra. de Ajalvir Km. 4, 28850 – Torrejón de Ardoz, Madrid, Spain

<sup>5</sup>Max-Planck-Institut für extraterrestrische Physik, Gießenbachstraße 1, 85748 Garching, Germany

<sup>6</sup>Centre for Astrophysics Research, Department of Physics, Astronomy and Mathematics, University of Hertfordshire, Hatfield, AL10 9AB, UK

<sup>7</sup>Institute of Astronomy, University of Cambridge, Madingley Road, Cambridge, CB3 0HA, UK

<sup>8</sup>Center for Astrophysics | Harvard & Smithsonian, 60 Garden St., Cambridge MA 02138 USA

<sup>9</sup>Department of Physics, University of Oxford, Denys Wilkinson Building, Keble Road, Oxford OX1 3RH, UK

<sup>10</sup>Scuola Normale Superiore, Piazza dei Cavalieri 7, I-56126 Pisa, Italy

Remaining affiliations are listed at the end of the paper

Accepted XXX. Received YYY; in original form ZZZ

## ABSTRACT

*JWST* spectroscopy has revealed a population of compact objects at redshifts  $z = 2-9$  with ‘v’-shaped spectral energy distributions, broad permitted lines, and, often, hydrogen Balmer absorption. Among these ‘Little Red Dots’ (LRDs), Abell2744-QSO1 at  $z = 7.04$  has been confirmed to have time-variable equivalent width (EW) in its broad emission lines, confirming its AGN nature. We extend the analysis of NIRSspec/IFS data from the BlackTHUNDER survey to the  $H\alpha$  line. The broad-line profile in Abell2744-QSO1 is manifestly non-Gaussian, requiring at least two Gaussian components with full width at half maximum  $FWHM = 450 \pm 50$  and  $1800 \pm 100$  km s<sup>-1</sup>. Crucially, we also detect a narrow-line Gaussian component, and strong  $H\alpha$  absorption (EW relative to the continuum  $\sim 30_{-9}^{+15}$  Å), confirming a connection between the strong Balmer break and line absorption. The absorber is at rest with respect to broad  $H\alpha$ , suggesting that the gas cannot be interpreted as an inflow or outflow, forming instead a long-lived structure. Its velocity dispersion is  $\sigma_{\text{abs}} = 100 \pm 10$  km s<sup>-1</sup>, consistent with the value inferred from the analysis of the Balmer break. Based on  $H\alpha$ , we infer a black hole mass of  $\log(M_{\bullet}/M_{\odot}) = 6.3-6.7$ , 0.9–1.3 dex smaller than previous estimates based on  $H\beta$ . The Eddington ratio is 0.7–1.6. Combining the high signal-to-noise ratio of the narrow  $H\alpha$  line with the spectral resolution  $R = 3,700$  of the G395H grating, we infer a narrow-line intrinsic dispersion  $\sigma_n = 22_{-6}^{+5}$  km s<sup>-1</sup>, which places a stringent constraint on the black-hole-to-dynamical-mass ratio of this system to be  $M_{\bullet}/M_{\text{dyn}} > 0.02-0.4$ . If  $M_{\bullet}$  is near the low-mass end of our estimates, the SMBH would be accreting at a super-Eddington rate. Alternatively, at the high- $M_{\bullet}$  end, there would be minimal room for a host galaxy.

**Key words:** galaxies: active – quasars: supermassive black holes – galaxies: high-redshift

## 1 INTRODUCTION

A key question in galaxy evolution is whether supermassive black holes (SMBHs) and their host galaxies grow in tandem or if one

forms first (Rees 1984; Latif & Ferrara 2016; Inayoshi et al. 2020). Did massive SMBH seeds emerge early, perhaps via direct collapse of pristine gas clouds (e.g., Bromm & Loeb 2003; Begelman et al. 2006), or did star clusters and proto-galaxies accumulate mass first, fuelling the growth of lower-mass seeds, for example via runaway collisions (e.g., Portegies Zwart et al. 1999)? This question is funda-

\* E-mail: francesco.deugenio@gmail.com

mental for our understanding of the link between SMBHs and galaxies. At redshifts  $z = 0-2$ , SMBH masses ( $M_{\bullet}$ ) correlate tightly with galaxy properties such as stellar velocity dispersion ( $M_{\bullet}-\sigma$  relation; Ferrarese & Merritt 2000; Gebhardt et al. 2000) and stellar or bulge mass ( $M_{\bullet}-M_{\star}$  relation; Kormendy & Ho 2013; McConnell & Ma 2013; Reines & Volonteri 2015, hereafter: RV15, Marconi & Hunt 2003; Saglia et al. 2016; Sun et al. 2025; Dalla Bontà et al. 2024, hereafter: DB25). These correlations suggest a co-evolutionary link, where accreting SMBHs regulate star formation through powerful feedback (Veilleux et al. 2005; Fabian 2012; Fiore et al. 2017; Veilleux et al. 2020), while galaxies, in turn, shape SMBH growth by modulating the gas supply for accretion, for instance by facilitating angular momentum loss, by altering the metal content and thermodynamic properties of the gas, and not least via star formation and supernova feedback (Dubois et al. 2015; Trebitsch et al. 2018; Silk 2017; Koudmani et al. 2022). While efficiently accreting SMBHs are readily observable at high redshifts powering Active Galactic Nuclei (AGN), the properties of their host galaxies remain uncertain – especially in the low-mass regime most relevant to understanding the origins of galaxies and SMBHs.

The advent of *JWST* enables direct observations of low-mass galaxies ( $M_{\star} > 10^6 M_{\odot}$ ) and SMBHs ( $M_{\bullet} > 10^6 M_{\odot}$ ) at  $z > 5$ , offering new insights into their co-evolution. Recent discoveries reveal a large population of accreting SMBHs in low-mass galaxies at these redshifts (Matthee et al. 2024), with many appearing over-massive relative to their hosts' stellar mass (e.g. Kocevski et al. 2023; Übler et al. 2023; Harikane et al. 2023; Kokorev et al. 2023; Maiolino et al. 2024b). While  $M_{\star}$  measurements in AGN-dominated systems remain uncertain, observations of faint SMBHs with low accretion rates support this trend (Carnall et al. 2023; Juodžbalis et al. 2024b). Notably, SMBHs at  $z > 5$  may still lie on the local  $M_{\bullet}-\sigma$  relation (Maiolino et al. 2024b), suggesting a degree of co-evolution *before* the onset of the local  $M_{\bullet}-M_{\star}$  relation, which may happen at later epochs and/or higher mass ranges (Sun et al. 2025; Li et al. 2025; McClymont W., in prep.).

In addition to a possible departure from local scaling relations, several broad-line AGN display strong Balmer breaks; if these spectral features arise from evolved stellar populations (a few hundred Myr and older), they would imply the existence of massive, old galaxies 600 Myr after the Big Bang (Wang et al. 2024a,b) with extremely high surface densities (Baggen et al. 2024; Ma et al. 2024). Alternatively, these Balmer breaks could arise from dense gas absorption (Inayoshi & Maiolino 2025) along the line of sight to the SMBH. The discovery of Abell2744-QSO1 (Furtak et al. 2023, 2024) enabled us to break this degeneracy. The continuum of this source cannot be well reproduced by stellar-population spectra alone (Ma et al. 2024, at least not without invoking *ad hoc* attenuation laws). Subsequent *JWST* observations have revealed that the equivalent widths (EW) of the broad lines are time variable (Ji et al. 2025, hereafter: J25; Furtak et al. 2025), ruling out a stellar origin (e.g., Baggen et al. 2024; Kokubo & Harikane 2024). Furthermore, time variability of the rest-frame optical continuum (J25) implies an AGN origin (but see Furtak et al. 2025 for a different view). Even more importantly, the narrow H $\beta$  and [O III] $\lambda$ 5007 emission lines impose an upper limit on  $M_{\text{dyn}}$  that is one order of magnitude lower than the  $M_{\star}$  inferred when assuming a stellar origin of the Balmer break.

One of the key predictions of J25 is that a strong, smooth Balmer break (with Balmer-break index  $\approx 2.3$ ; Inayoshi & Maiolino 2025) – associated with micro-turbulence of order  $100 \text{ km s}^{-1}$  – would produce equally strong Balmer line absorption with comparable broadening and high EWs. Indeed, several LRDs have been reported to display high-EW Balmer-line absorption (Matthee et al. 2024;

Wang et al. 2024a,b; Juodžbalis et al. 2024a; Taylor et al. 2024; Labbe et al. 2025). In contrast, in the stellar scenario, since micro-turbulence is relatively low ( $\lesssim 15 \text{ km s}^{-1}$  in the relevant stellar spectral types; Smith & Howarth 1998), line broadening is dominated by Gaussian-like stellar kinematics, resulting in significantly narrower line widths and much lower EWs (although non-Gaussian tails are still observed, due to pressure broadening). While J25 tentatively report H $\beta$  absorption, their measurement is only at the 3- $\sigma$  significance level, due to the low signal-to-noise ratio (SNR) of the underlying broad line. Confirming this absorption is crucial, because its presence is a key prediction of the gas-absorber hypothesis, and because, if present, it would enable probing the kinematics of the gas cloud.

In this work, we present a re-analysis of the BlackTHUNDER high-resolution NIRSpec observations from J25, focusing on the much brighter H $\alpha$  line, which we recover using a custom reduction procedure that extends beyond the nominal wavelength range calibration of NIRSpec. After describing the new data reduction and analysis (Section 2), we report three key findings (Section 3): non-Gaussian broad-H $\alpha$  emission, a strong rest-frame H $\alpha$  absorber, and an even more stringent upper limit on  $M_{\text{dyn}}$ . We conclude with a discussion of our results and their implications (Sections 4 and 5).

Throughout this work, we assume a flat  $\Lambda$ CDM cosmology from Planck Collaboration et al. (2020) and a Chabrier (2003) initial mass function. All EWs are in the rest frame.

## 2 DATA AND ANALYSIS

High-resolution spectroscopy of Abell2744-QSO1 covers H $\alpha$  at observed wavelength  $\lambda = 5.278 \mu\text{m}$  (spectral resolution  $R = 3,700$ ). These data were obtained by the programme Black holes in THE early Universe and their Dense surroundings (BlackTHUNDER; *JWST* proposal PID 5015; PIs H. Übler and R. Maiolino) using the NIRSpec spectrograph (Jakobsen et al. 2022) in integral field spectroscopy mode (IFS; Böker et al. 2022). Here we use only the G395H grating observations, consisting of 14 dithered integrations using the medium-dither cycling to offset fail-open shutters from the interlocking micro-shutter assembly (MSA; Ferruit et al. 2022; Bechtold et al. 2024). We used the improved reference sampling and subtraction (IRS<sup>2</sup>) readout mode (Rauscher et al. 2012), to minimize amplifier noise ('pink' or  $1/f$  noise; Moseley et al. 2010; Rauscher et al. 2017). Each integration consisted of 23 groups and one exposure, giving 1,692 s per dithered exposure and a total on-source exposure time of  $1692.3 \times 14 = 23,692 \text{ s}$ .

For the data reduction, we use the procedure described in Perna et al. (2023), but we start from the *JWST* pipeline version 1.17.1 and context file 1303. At  $z = 7.04$ , H $\alpha$  falls at  $\lambda = 5.278 \mu\text{m}$ , just outside the calibrated range of the NIRSpec G395H grating, which reaches  $\lambda < 5.27 \mu\text{m}$ . Moreover, the high-velocity wings of broad-H $\alpha$  emission can easily reach up to  $\lambda = 5.32 \mu\text{m}$ . However, since the low-pass F290LP is not suppressing long wavelengths, and since the grating transmission does not drop sharply, H $\alpha$  is readily observable on the detector. We therefore extract the data by extrapolating the flat-field curves and wavelength solution beyond the nominal range. Due to the small extrapolation (only 95 spectral pixels between  $\lambda = 5.27 \mu\text{m}$  and  $5.34 \mu\text{m}$ ), and thanks to the well characterized behaviour of the grating, the error on the wavelength solution is expected to be negligible. Similarly, the line-spread function is obtained from the grating equation, so we expect no significant deviation from the pre-flight characterization of the instrument (Jakobsen et al. 2022).

We extract the spectrum separately for the spectral regions around

[O III] $\lambda$ 4959 and H  $\alpha$ . To maximise the data quality, these apertures are smaller than the full-width at half-maximum (FWHM) of the point-spread function (PSF) at the relevant wavelength, with a radius of 0.125 and 0.15 arcsec, respectively. We applied aperture-loss corrections of 1.14 and 1.35 respectively, appropriate for a point source. The PSF analysis was performed on data from PID 2957 (PIs H. Übler and R. Maiolino), and will be presented in a future work.

The spectrum is shown in Fig. 1, with the data in black and the best-fit model in red. While the model is described in the next sections, here we observe that the continuum blueward and redward of H  $\alpha$  is described well by a linear fit, similar to other LRDs and broad-line AGN (over an equally narrow spectral range; e.g., Judžbalis et al. 2024b,a; Greene et al. 2024; Taylor et al. 2024). This agreement leads confidence to the accuracy of our extrapolated flux calibration. Nevertheless, since our  $M_{\bullet}$  measurements are sensitive primarily to the width of the broad H  $\alpha$ , with only a sub-linear dependence on the line flux, our main results are not driven by possible flux-calibration errors.

## 2.1 Spectral modelling

We model the narrow lines with Gaussians, using the same redshift and intrinsic velocity dispersion  $\sigma_n$  for all lines, but we convolve the model with the wavelength-dependent line spread function. Allowing for different intrinsic velocity dispersions between the H  $\beta$ –[O III] $\lambda$ 4959,5007 group and the H  $\alpha$ –[N II] $\lambda$ 6548,6583 group does not change our results. We further constrain the [O III] and [N II] $\lambda$ 6548,6583 doublet ratios to 0.336 (Storey & Zeppen 2000) and 0.328, respectively (Dojčinović et al. 2023), hence the narrow-line model requires seven parameters:  $z_n$ , two velocity dispersions, and the fluxes of H  $\beta$ , [O III] $\lambda$ 5007, H  $\alpha$  and [N II] $\lambda$ 6583. We model the continuum piecewise in each spectral window using a first-order polynomial each, requiring four parameters. For the broad Balmer lines we use a double Gaussian, given the clearly non-Gaussian shape of H  $\alpha$  (Fig. 1c). We remark that a double Gaussian is not necessarily associated with two physical components, and is used here as an effective way to reproduce the observed line profile. Alternative models using a single broad Gaussian or a Voigt profile are presented in Appendix A. The broad Gaussians have the same redshift, but we allow for a velocity offset between the broad and narrow lines. We have two independent FWHM values, while the flux is parametrized by the total unabsorbed flux of H  $\alpha$  and by the flux ratio between the narrowest Gaussian and the total unabsorbed line flux. There are thus five more free parameters. We consider these two FWHM values only as model parameters, without attaching a specific physical meaning. For each optimization step, we measure the total FWHM of the broad H  $\alpha$  from the sum of the two Gaussian profiles, without Balmer absorption. It is this derived value, dubbed  $FWHM_b(H\alpha)$ , which we use to estimate the physical properties of the system (Section 3.2). One additional parameter is required to model the broad H  $\beta$ , which also consists of two Gaussians, but their velocity, FWHM and flux ratio is the same as for H  $\alpha$ . The only additional parameter is the total unabsorbed H  $\beta$  flux. In principle, the flux ratio of the two broad Gaussians could be different between H  $\beta$  and H  $\alpha$ , for instance if these two Gaussians reflect different kinematic components, which could be subject to different excitation mechanisms and dust attenuation. However, the number of parameters for H  $\beta$  is effectively limited by the SNR of the data (J25). Finally, we add a dense hydrogen absorber, with a common covering factor  $C_f$ , the same velocity dispersion  $\sigma_{\text{abs}}$ , and the same velocity offset  $v_{\text{abs}}$  for H  $\beta$  and H  $\alpha$  (the velocity offset is relative to the redshift of the nearest narrow-line group). The residual intensity

at wavelengths  $\lambda$  is given by

$$I(\lambda)/I_0(\lambda) = 1 - C_f + C_f \cdot \exp(-\tau(k; \lambda)) \quad (1)$$

$$\tau(k; \lambda) = \tau_0(k) \cdot f[v(\lambda)],$$

where  $I_0(\lambda)$  is the spectral flux density before absorption,  $\tau_0(k)$  is the optical depth at the centre of the line (with  $k = \text{H}\beta$  or  $\text{H}\alpha$ ) and  $f[v(\lambda)]$  is the velocity distribution of the absorbing atoms, assumed to be a Gaussian probability distribution.  $I_0(\lambda)$  consists of both the continuum (dominated by the accretion disc; J25) and the BLR.

For model inference we use a Bayesian approach, with flat, non-informative priors around most parameters. The exceptions is the flux ratio  $F_n([\text{N II}]\lambda 6583)/F_n(\text{H}\alpha)$ , which we bias to be  $< 1$  using an informative probability prior. This modelling choice enables us to correctly account for the additional uncertainties on the model parameters due to possible [N II] $\lambda$ 6548,6583 emission, while enforcing the observationally established weakness of this doublet at  $z > 5$ , including in clear broad-line AGN (e.g., Übler et al. 2023). The adopted prior uses the complementary error function, centred at 1 and with scale parameter  $\sigma = 0.1$ , truncated between 0 and infinity. The posterior probabilities are sampled using the Markov Chain Monte Carlo method (see D’Eugenio F., in prep. for more details).

## 3 RESULTS

The maximum-likelihood model is shown in Fig. 1. The H  $\alpha$  narrow line is clearly detected, with the observed flux  $F_n(\text{H}\alpha)$  being more than  $8\sigma$  away from 0 (Table 1). Together with weaker H  $\beta$  and [O III] $\lambda$ 5007, the observed wavelength of narrow H  $\alpha$  implies a redshift  $z = 7.0367 \pm 0.0001$ . The intrinsic width of the narrow lines is extremely small,  $\sigma_n = 22^{+5}_{-6} \text{ km s}^{-1}$ , corresponding to 0.6 times the spectral resolution ( $FWHM = 81 \text{ km s}^{-1}$ ,  $\sigma_R = 34 \text{ km s}^{-1}$  at the observed wavelength of H  $\alpha$ ). While the inferred  $\sigma_n$  is small, a simple analytical calculation tells us that, given a Gaussian LSF with  $R = 3,700$  and a line detection with SNR of 8, we can detect a spectral broadening of  $\sigma = 22 \text{ km s}^{-1}$  at  $4.8\sigma$  (Zhou et al. 2017); this statistical significance is slightly better yet comparable to the width of the posterior probability on  $\sigma_n$  (i.e.,  $22/6 = 3\text{-}\sigma$  significance). The larger uncertainties for our measured  $\sigma_n$  relative to the analytical prediction can easily be explained by the presence of additional unknowns compared to the analytic approximation of Zhou et al. (2017), such as the absorber depth and redshift. We find no evidence of [N II] $\lambda$ 6548,6583, with  $F_n([\text{N II}]\lambda 6583)/F_n(\text{H}\alpha) < 0.16$  ( $3\sigma$ ).

The broad H  $\alpha$  requires two Gaussians (see Appendix A). The flux ratio between the narrowest of these broad components and the total broad H  $\alpha$  is  $0.41^{+0.04}_{-0.03}$ . Note that a Voigt profile – which also captures a pure Lorentzian profile, due to the finite instrument resolution – does not seem to reproduce the data (Appendix A). The width of the narrowest and broadest Gaussians are  $FWHM = 450^{+50}_{-50} \text{ km s}^{-1}$  and  $1800^{+100}_{-90} \text{ km s}^{-1}$ .

### 3.1 Host galaxy

To estimate the dynamical mass of the system, we use the same approach as J25, but we leverage the higher spectral resolution and SNR of H  $\alpha$  to infer a more accurate velocity dispersion  $\sigma_n = 22 \text{ km s}^{-1}$  of the gas. For the galaxy size, we adopt the upper limit on the half-light radius  $R_e < 30 \text{ pc}$  from Furtak et al. (2023). Our highest estimate of  $M_{\text{dyn}}$  is derived from the virial calibration of van der Wel et al. (2022),  $M_{\text{dyn}} = K(n)K(q)\sigma_{\text{int}}^2 R_{\text{SMA}}/G$ , where  $K(n)$  and  $K(q)$  are functions of the Sérsic index  $n$  and the projected axis ratio

**Table 1.** Summary of the emission-lines model of Abell2744-QSO1, reporting the median and 16<sup>th</sup>–84<sup>th</sup> percentile range of the posterior probability distribution on 17 parameters of the model (Section 2; four free parameters for the continuum are not listed). The ‘n’ and ‘b’ subscripts denote values inherent to the narrow lines and to the (two-component) broad lines, respectively.

Observable	Posterior	Unit
$\mu F_n([\text{O III}]\lambda 5007)^a$	$0.07^{+0.02}_{-0.02}$	$[10^{-18} \text{ erg s}^{-1} \text{ cm}^{-2}]$
$\mu F_n(\text{H}\beta)$	$0.11^{+0.02}_{-0.02}$	$[10^{-18} \text{ erg s}^{-1} \text{ cm}^{-2}]$
$\mu F_n(\text{H}\alpha)$	$0.54^{+0.08}_{-0.07}$	$[10^{-18} \text{ erg s}^{-1} \text{ cm}^{-2}]$
$\mu F_n([\text{N II}]\lambda 6583)$	$< 0.16$	$[10^{-18} \text{ erg s}^{-1} \text{ cm}^{-2}]$
$\sigma_n$	$22^{+5}_{-6}$	$[\text{km s}^{-1}]$
$z_n$	$7.0367^{+0.0001}_{-0.0001}$	$[-]$
$v_b$	$-19^{+8}_{-10}$	$[\text{km s}^{-1}]$
$F_b(\text{H}\beta)/F_b(\text{H}\alpha)$	$0.10^{+0.01}_{-0.01}$	$[-]$
$\mu F_b(\text{H}\alpha)$	$13^{+2}_{-1}$	$[10^{-18} \text{ erg s}^{-1} \text{ cm}^{-2}]$
$F_{b,1}/F_b(\text{H}\alpha)$	$0.41^{+0.04}_{-0.03}$	$[-]$
$FWHM_{b,1}(\text{H}\alpha)^b$	$450^{+50}_{-50}$	$[\text{km s}^{-1}]$
$FWHM_{b,2}(\text{H}\alpha)$	$1800^{+100}_{-90}$	$[\text{km s}^{-1}]$
$v_{\text{abs}}$	$-36^{+9}_{-10}$	$[\text{km s}^{-1}]$
$\sigma_{\text{abs}}$	$100^{+10}_{-10}$	$[\text{km s}^{-1}]$
$C_f$	$0.55^{+0.07}_{-0.07}$	$[-]$
$\tau_0(\text{H}\beta)$	$20^{+7}_{-8}$	$[-]$
$\tau_0(\text{H}\alpha)$	$1.9^{+0.7}_{-0.6}$	$[-]$

<sup>a</sup> The line fluxes are not corrected for lensing magnification nor for dust attenuation (see Table 2 for the corrected values).

<sup>b</sup> The FWHM values reported here are model parameters for the two Gaussians representing the broad Balmer lines, and are not physical parameters. The total FWHM relevant as a physical parameter is reported in Table 2.

$q$ ,  $R_{\text{sma}}$  is the semi-major axis and  $\sigma'_{\star, \text{int}}$  is the integrated stellar velocity dispersion. Assuming a Sérsic index  $n = 1$  and axis ratio  $q = 1$  leads to the highest possible value of the structural factor  $K(n)K(q)$  in this calibration, hence the most conservative upper limit on  $M_{\text{dyn}}$  from the van der Wel et al. (2022) calibration. We also increase  $\sigma_n$  by 0.2 dex, following the calibration of Bezanson et al. (2018), as described in Übler et al. (2023) and Maiolino et al. (2024b). This is meant to capture the different average value of  $\sigma$  between gas and stars (the latter of which underlies the calibration of van der Wel et al. 2022). However, we note that at low values of the stellar velocity dispersion, the calibration of Bezanson et al. (2018) may already implicitly capture an average inclination correction, since aperture velocity dispersion has a larger velocity contribution for gas than for stars (e.g., Cortese et al. 2016; Barat et al. 2019). Our inclusion of the Bezanson et al. (2018) scaling between the gas and stellar aperture dispersions thus yields an even more conservative upper limit on  $M_{\text{dyn}}$ , by 0.4 dex. With this approach, we find an upper limit  $\log(M_{\text{dyn}}/M_{\odot}) < 8.0$ . Alternatively, using the calibration of Stott et al. (2016) for purely dispersion dominated systems, we find  $\log(M_{\text{dyn}}/M_{\odot}) < 7.1$ . These are extremely low values, driven by the low dispersion of the narrow H  $\alpha$  and by the unresolved nature of the galaxy in the spatial dimension.

From the observed Balmer decrement of the narrow lines, we derive a dust attenuation value  $A_{V,n} = 1.4 \pm 0.4$  mag (Table 2). We adopted the Gordon et al. (2003) dust extinction law and an intrinsic H  $\alpha$ /H  $\beta$  flux ratio of 2.86, appropriate for Case-B recombination, electron temperature  $T_e = 10,000$  K and density  $n_e = 500 \text{ cm}^{-3}$ . This value is inconsistent with the blue UV slope (Witten C., in prep.), suggesting a different origin for the narrow lines and rest-frame UV continuum, with the latter perhaps due to the AGN itself (J25).

For the BLR, assuming an intrinsic Balmer decrement of 3.1

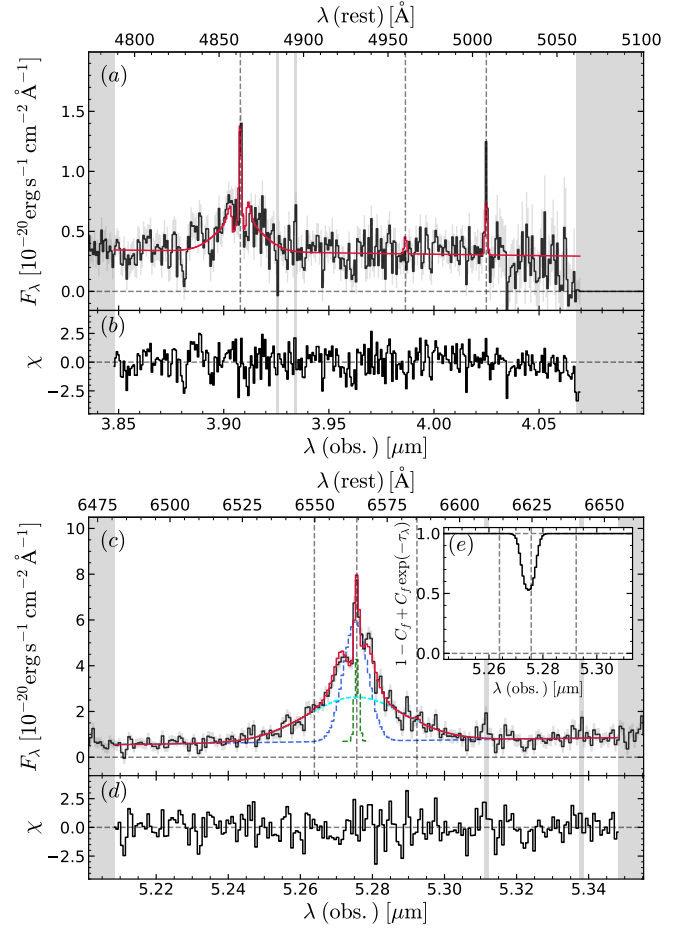


**Figure 1.** Detail of the BlackTHUNDER aperture spectrum (black) around H  $\beta$  and [O III] $\lambda$ 4959,5007 (panel a) and H  $\alpha$  (panel c). The red line is the maximum-likelihood model (Section 2), with the  $\chi$  residuals shown in panels b and d. The maximum-likelihood model includes the continuum and two broad Gaussians, subject to Balmer-line absorption, and a unabsorbed narrow Gaussian. For H  $\alpha$ , we show the narrow-component Gaussian in green and the two un-absorbed broad Gaussians in cyan and blue. There is clear evidence of line absorption in H  $\alpha$  and of a narrow component with  $\sigma_n = 24 \text{ km s}^{-1}$ . The absorption profile (including partial covering factor) is shown in panel e.

(Dong et al. 2008), we find  $A_{V,b} = 3.1 \pm 0.3$  mag. We caution, however, that the intrinsic H  $\alpha$ /H  $\beta$  ratio in BLRs is quite uncertain, reaching values up to 10 (Ilić et al. 2012). For Abell2744-QSO1 we disfavour such a high intrinsic ratio, because the observed Balmer decrement of the broad lines is also equal to  $10 \pm 1$ . Given this observed value, assuming an intrinsic decrement of 10 would imply little or no dust attenuation, at variance with the considerable dust found in both the narrow lines as well as in front of the accretion disc ( $A_V = 2.13 \pm 0.02$  mag; J25).

Based on the dust-corrected H  $\alpha$  luminosity of the narrow component and using the star-formation rate (SFR) scaling of McClymont et al. (2025), we infer  $2.5^{+1.2}_{-0.8} M_{\odot} \text{ yr}^{-1}$  (corrected for lensing using  $\mu = 5.8$ ; Furtak et al. 2023). Using the calibration of Shapley et al. (2023), we would infer instead a much lower value of  $0.35^{+0.16}_{-0.12} M_{\odot} \text{ yr}^{-1}$ . This value assumes that the narrow-line region is completely dominated by star formation photo-ionization, with no AGN contribution. Clearly, since Abell2744-QSO1 is AGN dominated (J25), a more cautious approach would be to regard this SFR estimate as an upper limit. On the other hand, we would reach the opposite conclusion (i.e., negligible AGN contribution) from the width

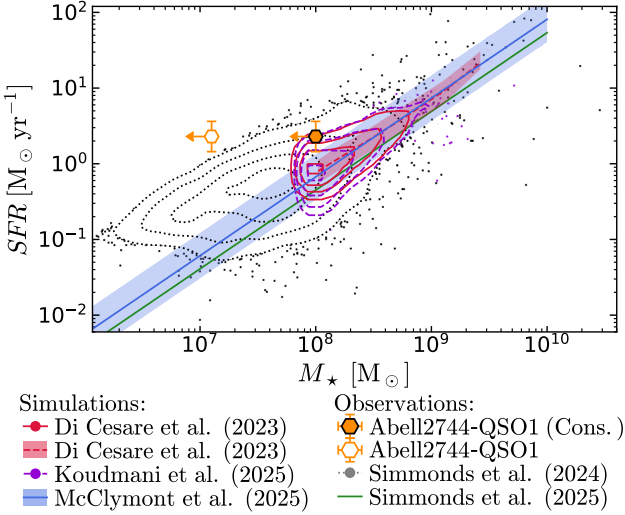


**Figure 2.** Abell2744-QSO1 in relation to the SFMS, using our largest upper limit on  $M_{\text{dyn}}$  as an upper limit on  $M_{\star}$  too, and assuming that all the narrow H $\alpha$  is due to star formation. The empty (filled) hexagons use the lowest and highest (most conservative) estimate of  $M_{\text{dyn}}$ . Solid and dashed contours are simulated galaxies at  $z = 7-7.5$  from DUSTYGADGET (Graziani et al. 2020; Di Cesare et al. 2023) and from AESOPICA (Koudmani et al. 2022; Koudmani et al., in prep.). The dashed-red and solid-blue lines with shaded 0.2–0.3 dex scatter are the SFMS from the Di Cesare et al. (2023) and from the THESAN-ZOOM project (Kannan et al. 2025; McClymont et al. 2025). The dotted contours are observed galaxies at  $6.5 \leq z < 7.5$  from JADES (Simmonds et al. 2024), with the green line representing a bias-corrected SFMS model (Simmonds et al., in prep.). Abell2744-QSO1 (orange hexagons) lies conservatively near the top edge of the SFMS. While this location (and the upper limit on  $M_{\star}$ ) seemingly imply a starburst nature, any AGN contribution to H $\alpha$  would lower the estimated SFR.

of the narrow lines. The extremely narrow value of  $\sigma_n$  suggests that the narrow lines arise relatively far from the central few pc. For example, assuming that the enclosed mass was solely due to the SMBH (we adopted  $M_{\bullet} = 10^{6.7} M_{\odot}$ , see Section 3.2), the virial velocities at 3 and 10 pc from the centre are  $120 \text{ km s}^{-1}$  and  $65 \text{ km s}^{-1}$ , respectively. From the narrow-H $\alpha$  luminosity, assuming  $T_e = 10,000 \text{ K}$ , we can estimate the gas mass as

$$M_{\text{H}\alpha} = 3.3 \times 10^8 M_{\odot} \frac{L_n(\text{H}\alpha)}{10^{43} \text{ erg s}^{-1}} \frac{100 \text{ cm}^{-3}}{n_e}. \quad (2)$$

For an electron density in the range  $100-500 \text{ cm}^{-3}$ , plausible for star-forming regions, we obtain a ionized-gas mass of  $2-10 \times 10^7 M_{\odot}$ , comparable to the range of dynamical masses. Higher densities such as those found in the absorber and in the BLR would significantly lower this estimate, but as we have seen, the small velocity dispersion of the narrow lines disfavours their origin too close to the BLR. At face value, these gas masses leave almost no room for stars in Abell2744-QSO1. Dark matter should also be negligible on these scales. For an object with  $M_{\star} < M_{\text{dyn}} < 10^{7.1}-10^8 M_{\odot}$ , the halo mass at  $z = 7$  should be of order  $M_h < 10^{10.9}-10^{11.3} M_{\odot}$ . Using the relations from Bullock et al. (2001) and Dutton & Macciò (2014), we can infer the scale density and scale radius, from which we derive the dark-matter mass inside the sphere of radius 30 pc to be  $M_h(R < 30 \text{ pc}) < 3 \times 10^6 M_{\odot}$ .

With the measured SFR, and using the upper limit on  $M_{\text{dyn}}$  as a limit on  $M_{\star}$  too, we can relate this object to the star-forming main sequence of galaxies (SFMS). In Fig. 2 we show the position of Abell2744-QSO1 relative to star-forming galaxies at  $z = 7.04$ , from

both observations and numerical simulations. Observational data are from the JWST Advanced Deep Extragalactic Survey (JADES; Eisenstein et al. 2023; Rieke et al. 2023; Hainline et al. 2024), where  $M_{\star}$  and SFR were measured from spectral energy distribution (SED) modelling (Simmonds et al. 2024). Simulated galaxies are from the hydrodynamic suites DUSTYGADGET (Graziani et al. 2020; Di Cesare et al. 2023), THESAN-ZOOM (Kannan et al. 2025; McClymont et al. 2025), and AESOPICA (Koudmani et al. 2022; Koudmani et al., in prep.). AESOPICA is a new suite of large-volume cosmological simulations (Koudmani et al., in prep) built upon the FABLE galaxy formation model (Henden et al. 2018), with targeted updates for modelling the growth of infant SMBHs in the early Universe. AESOPICA explores three key modifications to fiducial galaxy formation models: enabling efficient accretion in the low-mass regime (Koudmani et al. 2022), incorporating super-Eddington accretion, and examining a broad range of seed masses ( $10^2 M_{\odot}$  to  $10^5 M_{\odot}$ ) following seed evolution from early cosmic epochs ( $z \sim 20$ ).

Assuming that all the narrow H $\alpha$  was due to star formation, we would infer a location of Abell2744-QSO1 near the 1- $\sigma$  edge above the SFMS, as inferred from all of DUSTYGADGET, THESAN-ZOOM, and AESOPICA. However, using the less conservative mass estimate of  $\log(M_{\star}/M_{\odot}) < 7.1$ , Abell2744-QSO1 would lie clearly outside the range of simulated galaxies, possibly representing a challenge for current models of SMBH and galaxy growth. Considering the more stringent upper limit on  $M_{\text{dyn}}$  (and hence on  $M_{\star}$ ) from the Stott et al. (2016) calibration, we would infer that Abell2744-QSO1 lies above the SFMS even for an AGN contribution as high as 90% (open hexagon in Fig. 2). If confirmed, this would suggest a link between overmassive black holes and starbursts. Clearly, an independent measure of the SFR is required to disentangle the AGN contribution, and to assess the precise star-forming nature of the host galaxy.

### 3.2 Black hole mass

To estimate the mass of the SMBH, we use two alternative virial calibrations, both based on the luminosity and width of the broad H $\alpha$  line. The calibration of RV15 uses the line FWHM. In our case, we adopt the FWHM of the total line profile (modelled as the sum of two Gaussians), and corrected for line absorption. With this method, and with  $FWHM_b = 560 \pm 70 \text{ km s}^{-1}$  (Table 2), we infer  $\log(M_{\bullet}^{\text{RV15}}/M_{\odot}) = 6.1_{-0.1}^{+0.1}$ , with 0.3 dex additional uncertainty from the scatter about the calibration. Upscaling for the dust attenuation inferred from the narrow lines, the black hole mass increases by 0.2 dex. These values are much lower than previous estimates based on the width of the broad H $\beta$  line (Furtak et al. 2024; J25,  $FWHM_b(\text{H}\beta) = 2658_{-292}^{+351} \text{ km s}^{-1}$ ); the key difference is the much narrower FWHM of the total broad line profile (Table 2). Our total  $FWHM_b(\text{H}\alpha)$  (Table 2) is much closer to the FWHM of the narrowest of the two broad Gaussians ( $FWHM_{b,1} = 450 \pm 50 \text{ km s}^{-1}$  vs  $FWHM_{b,2} = 1,800_{-90}^{+100} \text{ km s}^{-1}$ ; Table 1), but this is a consequence of the flux ratio between the two components.

As an alternative, we use a calibration based on the line second moment,  $\sigma_{\text{lb}}$ , which we measured on the observed line profile after subtracting the continuum. We remark that  $\sigma_{\text{lb}}$  is not the dispersion of the Gaussian. In fact, we find  $\sigma_{\text{lb}} = 720_{-120}^{+100} \text{ km s}^{-1}$ , larger than  $FWHM_b(\text{H}\alpha)$ . This larger value is due to a combination of model assumptions (the  $\sigma_{\text{lb}}$  method does not take into account the presence of the absorber) and to the broad wings of H $\alpha$ , which are up-weighted when calculating the second-moment of the line profile. For reference,  $\sigma_{\text{lb}}$  diverges for a Lorentzian-like line profile. From our estimate of  $\sigma_{\text{lb}}$ , using the calibration of DB25, we obtain

$\log(M_{\bullet}^{\text{DB25}}/M_{\odot}) = 6.5_{-0.2}^{+0.1}$ , with 0.2 dex calibration uncertainties. Correcting for dust attenuation we get  $\log(M_{\bullet}^{\text{DB25}}/M_{\odot}) = 6.7_{-0.2}^{+0.2}$ .

To obtain the bolometric luminosity, we use the calibration of [Stern & Laor \(2012\)](#), based on the broad H $\alpha$ , and find  $L_{\text{bol}} = 4 \times 10^{44}$  erg s $^{-1}$ , within a factor of 2 from the value based on broad H $\beta$ , and within a factor of 3 from the value based on the continuum at 5,100 Å ([J25](#)). The resulting Eddington ratios range from  $\lambda_{\text{Edd}}^{\text{DB25}} = 0.4_{-0.1}^{+0.2}$  to  $\lambda_{\text{Edd,ism}}^{\text{RV15}} = 1.6_{-0.5}^{+0.8}$  (Table 2). These are much higher than what was reported previously based on H $\beta$  ( $\lambda_{\text{Edd}}^{\text{DB25}} = 0.05\text{--}0.24$ ; [Furtak et al. 2024, J25](#)), with the increase in  $\lambda_{\text{Edd}}$  driven primarily by the decrease in  $M_{\bullet}$ , since our  $L_{\text{bol}}$  is comparable with previous estimates.

### 3.3 Absorbing gas

The gas absorber has a very high equivalent width; when measured relative to the broad-H $\alpha$  flux, the value is  $EW(\text{H}\alpha) = 6_{-1}^{+1}$  Å, while the value measured relative to the continuum is  $EW_{\text{cont}}(\text{H}\alpha) = 30_{-9}^{+15}$  Å. Both values are very high, but the second value is so high that it completely rules out a stellar origin<sup>1</sup>. The strength of the H $\beta$  absorber appears much larger, with an optical depth at the line centre of  $\tau_0(\text{H}\beta) = 20_{-8}^{+7}$ , compared to only  $\tau_0(\text{H}\alpha) = 1.9_{-0.6}^{+0.7}$ . Since these are absorption lines arising from the same energy level, their optical depth ratios are set by atomic physics to be  $\tau_0(\text{H}\beta)/\tau_0(\text{H}\alpha) = \lambda_{\text{H}\beta}/\lambda_{\text{H}\alpha} \cdot f_{2\rightarrow4}/f_{2\rightarrow3} = 0.137$ , where we used the oscillator strength values  $f_{2\rightarrow4} = 0.119$  and  $f_{2\rightarrow3} = 0.641$ . Our results yield  $\tau_0(\text{H}\beta)/\tau_0(\text{H}\alpha) = 11 \pm 6$ , almost 2- $\sigma$  away from the theoretical value. Higher-quality observations of H $\beta$  are needed to confirm this finding, but, at face value, it suggests the presence of some line infill. Spatially, the absorber is clearly located in the BLR, or between the BLR and the observer, as demonstrated in Fig. 3; there is clearly not enough continuum flux to be absorbed, and the model is unable to reproduce the data.

The mean velocity offset of the BLR model is  $v_b = -19 \pm 8$  km s $^{-1}$ , with a significance of only 2.5  $\sigma$ , which we find no strong evidence for a velocity offset, given that we miss the peak of the BLR due to the absorption. The velocity of the absorber is also very close to the systemic velocity,  $v_{\text{abs}} = -36_{-10}^{+9}$  km s $^{-1}$  (4  $\sigma$ ). This weak blueshift echoes the blueshift of the BLR, such that their difference is fully consistent with 0 (within 1.1  $\sigma$ ), implying that the dense-gas absorber is at rest relative to the BLR.

While a single rest-frame absorber could indicate an inflow/outflow directed close to the plane of the sky, there is increasing evidence for near rest-frame absorbers being common, favouring stationary equilibrium, such as a gas disc, or at least long-lived structures, such as stalling gas clouds. Indeed, if we adopt the column density  $N_{\text{H}} \sim 10^{24}$  cm $^{-2}$  estimated from the strength of the Balmer absorption ([J25](#)), the gas absorber could be long-lived even under a high- $\lambda_{\text{Edd}}$  scenario, because the cross section for absorption depends on the dust fraction ([Fabian et al. 2008](#)), which we estimate to be low. In fact, from the dust-to-column density ratio of the Milky Way and from the hydrogen column density of [J25](#), we can derive constraints on the dust and metallicity properties of the absorbing gas.

<sup>1</sup> High-EW Balmer-line absorption in stellar atmospheres is routinely observed in spectral types from late B to early F, but is never as strong as seen here. For reference, for a simple stellar population employing MIST isochrones ([Choi et al. 2016](#)) and the C3K model atmospheres ([Conroy et al. 2019](#)), the maximum  $EW(\text{H}\alpha)$  is 8.3 Å for a burst age of 400–500 Myr, depending on metallicity. For Abell2744-QSO1, such an old burst age is ruled out by the amount of rest-UV light.

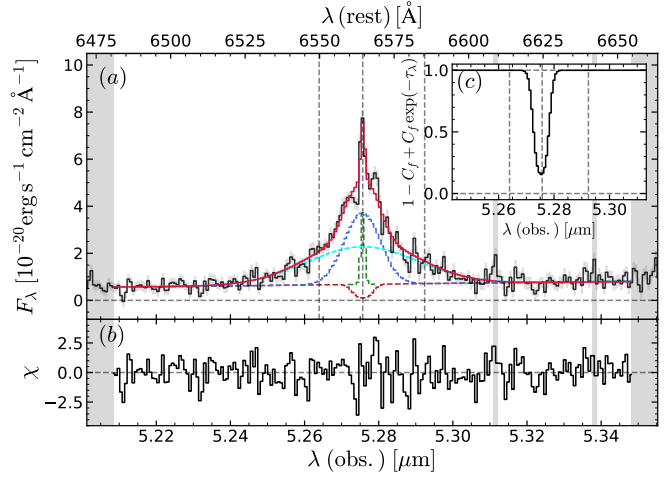


**Figure 3.** The best-fit model where the dense gas absorbs only the continuum and not the broad H $\alpha$  line cannot reproduce the observations, therefore the dense absorber must be located between the observer and the BLR.

Following the method of [D'Eugenio et al. \(2024, their eq. 1\)](#), we can write

$$Z \cdot \xi_d = Z_{\text{MW}} \cdot \xi_{d,\text{MW}} \frac{A_{V,n}}{N_{\text{H}}} \left( \frac{N_{\text{H}}}{A_V} \right)_{\text{MW}}, \quad (3)$$

where  $Z$  is the ISM metallicity,  $\xi_d$  is the dust-to-metal ratio. Adopting the Milky-Way (MW) values of the gas-to-extinction ratio  $N_{\text{H}}/A_V = 2.09 \pm 0.03$  cm $^{-2}$  mag $^{-1}$  ([Zhu et al. 2017](#)), the dust-to-metal ratio  $\xi_{d,\text{MW}} = 0.45$  ([Konstantopoulou et al. 2024](#)), and an ISM metallicity in the solar neighbourhood  $Z_{\text{MW}} = 0.6 Z_{\odot}$  ([Arellano-Córdova et al. 2021](#)), we infer  $Z \cdot \xi_d \lesssim 0.0008$ . The inequality derives from the fact that some or even most of the attenuation we inferred from the narrow lines  $A_{V,n}$  may not be associated with the absorber. Such a low value of  $Z \cdot \xi_d$  implies that the absorbing medium is extremely dust poor. This could stem in part from low metallicity, and in part due to a very low value of  $\xi_d$ , which would be expected if the absorber is within the dust sublimation radius from the SMBH, and which resonates with the relatively large  $\lambda_{\text{Edd}}$  value. Such a conclusion would lower the effective Eddington ratio for the galaxy ISM, thus increasing the lifetime of absorbing clouds ([Fabian et al. 2008; Arakawa et al. 2022](#)).

## 4 DISCUSSION

‘Little Red Dots’ defined as having broad permitted lines, a ‘v-shaped’ SED and very compact morphology are a puzzling new class of AGN, unknown before *JWST*. It is clear that these objects are preferentially inherent to the Universe before Cosmic Noon, at  $z > 2\text{--}3$ ; with only two known ‘low-redshift’ cases at  $z = 2.3$  ([Juodžbalis et al. 2024a](#)) and  $z = 3.1$  ([Wang et al. 2024a](#)).

Abell2744-QSO1 ([Furtak et al. 2023, 2024](#)) was found to have one of the strongest Balmer breaks observed at high redshift (see also [Labbe et al. 2025](#)). The smooth nature of the break in this galaxy has defied any attempt to model it as a stellar Balmer break ([Ma et al. 2024](#)). In contrast, by using the model of [Inayoshi & Maiolino \(2025\)](#), which associates the Balmer break to dense gas absorbers around the AGN, and by introducing a large micro-turbulence parameter of  $v_t \sim 120$  km s $^{-1}$ , [J25](#) were able to successfully model the shape of the continuum break.

**Table 2.** Summary of the derived parameters of Abell2744-QSO1, reporting the median and 16<sup>th</sup>–84<sup>th</sup> percentile range of the posterior probability distribution. All fluxes are corrected for dust reddening, and all relevant quantities have been corrected for gravitational lensing magnification (assuming  $\mu = 5.8$ ; Furtak et al. 2023). The ‘n’ and ‘b’ subscripts denote values inherent to the narrow lines and to the (two-component) broad lines, respectively.

Property	Posterior	Unit
$A_{V,n}$	$1.4^{+0.4}_{-0.4}$	[mag]
$A_{V,b}$	$3.1^{+0.3}_{-0.3}$	[mag]
$F_n(\text{H}\beta)$	$0.09^{+0.05}_{-0.03}$	[ $10^{-18}$ erg s $^{-1}$ cm $^{-2}$ ]
$F_n(\text{[OIII]}\lambda 5007)$	$0.05^{+0.04}_{-0.02}$	[ $10^{-18}$ erg s $^{-1}$ cm $^{-2}$ ]
$F_n(\text{H}\alpha)$	$0.27^{+0.13}_{-0.09}$	[ $10^{-18}$ erg s $^{-1}$ cm $^{-2}$ ]
$L_n(\text{H}\alpha)$	$0.16^{+0.08}_{-0.05}$	[ $10^{42}$ erg s $^{-1}$ ]
$SFR(\text{H}\alpha)^a$	$2.5^{+1.2}_{-0.8}$	[ $M_\odot$ yr $^{-1}$ ]
$EW_{\text{abs}}(\text{H}\beta)$	$9.0^{+0.7}_{-0.7}$	[ $\text{\AA}$ ]
$EW_{\text{abs}}(\text{H}\alpha)$	$6^{+1}_{-1}$	[ $\text{\AA}$ ]
$EW_{\text{cont}}(\text{H}\beta)$	$11^{+4}_{-3}$	[ $\text{\AA}$ ]
$EW_b(\text{H}\beta)$	$-36^{+6}_{-3}$	[ $\text{\AA}$ ]
$EW_{\text{cont}}(\text{H}\alpha)$	$30^{+15}_{-9}$	[ $\text{\AA}$ ]
$EW_b(\text{H}\alpha)$	$-170^{+10}_{-20}$	[ $\text{\AA}$ ]
$F_b(\text{H}\beta)$	$0.9^{+0.7}_{-0.4}$	[ $10^{-18}$ erg s $^{-1}$ cm $^{-2}$ ]
$F_b(\text{H}\alpha)$	$5^{+2}_{-1}$	[ $10^{-18}$ erg s $^{-1}$ cm $^{-2}$ ]
$FWHM_b(\text{H}\alpha)$	$560^{+70}_{-70}$	[km s $^{-1}$ ]
$\sigma_{1,b}(\text{H}\alpha)^b$	$720^{+100}_{-120}$	[km s $^{-1}$ ]
$\log M_{\bullet, \text{ism}}^{\text{RV15}}$	$6.3^{+0.1}_{-0.1}$	[dex $M_\odot$ ]
$\log M_{\bullet, \text{ism}}^{\text{DB25}}$	$6.7^{+0.2}_{-0.2}$	[dex $M_\odot$ ]
$\lambda_{\text{Edd,ism}}^{\text{RV15}}$	$1.6^{+0.8}_{-0.5}$	[—]
$\lambda_{\text{Edd,ism}}^{\text{DB25}}$	$0.7^{+0.4}_{-0.2}$	[—]

<sup>a</sup> This SFR assumes no AGN contribution, so should be regarded as an upper limit.

<sup>b</sup>  $\sigma_{1,b}$  is the second moment of the observed line profile, as described in Peterson et al. (2004) and DB25. It shall not be confused with the dispersion of a Gaussian.

#### 4.1 Properties of the gas absorber

One of the key predictions of the Inayoshi & Maiolino (2025) model is the presence of high-EW Balmer-line absorption. While J25 reported tentative evidence of H $\beta$  absorption, the much higher SNR of the H $\alpha$  emission line enables us not only to confirm beyond any doubt that Abell2744-QSO1 also has H $\alpha$  absorption (Fig. 1), but also to study its kinematics. The EW of this absorption is too large to be of stellar origin, completely ruling out a stellar-atmosphere interpretation of the Balmer break. The inferred broadening,  $\sigma_{\text{abs}} = 100 \pm 10$  km s $^{-1}$ , closely matches the micro-turbulence value required to model the continuum shape (by definition  $v_t \equiv \sqrt{2}\sigma_{\text{abs}}$ ). Such a high degree of smoothness cannot be obtained from stellar atmospheres ( $v_{\text{turb}} \lesssim 15$  km s $^{-1}$ ; Smith & Howarth 1998), or from stellar kinematics (given the Gaussian dependence of kinematics-driven broadening, while turbulence-driven broadening is exponential).

Different aspects of our analysis favour a location of the absorber within or just outside the BLR. First, because the absorption is too deep to absorb only the continuum (in agreement with the ‘Rosetta Stone’ LRD from Juodžbalis et al. 2024a). Second, the density of the absorber is fully consistent with the high densities of BLRs (J25). Finally, by combining the column density from J25 with our own measurement of  $A_{V,n}$ , we derive an upper limit on the product  $Z \cdot \xi_d \lesssim 0.0008$ , indicating very little dust in the gas absorber. But dust is certainly present in Abell2744-QSO1 (from both the Balmer decrement of the narrow lines and from the continuum analysis Furtak et al. 2024; Ma et al. 2024; J25). A location of the gas absorber inside the dust-sublimation radius of the SMBH, i.e. the BLR and its immediate vicinity, would naturally explain why this gas lacks any significant dust, unlike the rest of the system.

#### 4.2 Absorber energetics

The high value of the turbulence (now coming from two independent measurements) must indicate either a transient nature, or an adequate energy source to counteract dissipation. We can obtain a crude estimate of the clouds turbulent-energy density roughly as  $1.4m_p n_H \cdot \sigma_{\text{abs}}^2$ , with  $n_H = 10^{8.5} - 10^{10}$  cm $^{-3}$  (J25). For a spherical shell of radius  $R_c$ , thickness  $\delta R_c$  and solid angle  $\Omega_c$ , the total turbulent energy becomes

$$E_c = 6.9 \times 10^{50} \left( \frac{\Omega_c}{4\pi} \right) \left( \frac{n_H}{10^8 \text{cm}^{-3}} \right) \left( \frac{R_c}{1 \text{pc}} \right)^2 \left( \frac{\delta R_c}{0.001 \text{pc}} \right) \left( \frac{\sigma_{\text{abs}}}{100 \text{km s}^{-1}} \right)^2 \text{erg}. \quad (4)$$

For the galacto-centric distance of the clouds  $R_c$  we use the size of the BLR; since there is not enough continuum to be absorbed (Section 3.3), the clouds must be back-illuminated by the BLR, at least in part. We set therefore a lower limit  $R_c = R_{\text{BLR}} > 2.7$  pc, where the lower bound on the size of the BLR has been derived from the time delay between the continuum and emission-line variability (J25). The thickness of the clouds is not known for the object in hand, but it has been estimated to be  $\delta R_c < 10^{-3}$  pc in a low-redshift LRD (Juodžbalis et al. 2024a). With these numbers and setting  $\Omega_c = 4\pi$ , the turbulent energy of the absorbing clouds is  $E_c \sim 10^{52} - 10^{53}$  erg. Under the assumption of a long-lived cloud, we can estimate the power required to maintain the turbulence as  $P_c \sim E_c / (\delta R_c / \sigma_{\text{abs}})$ , or

$$P_c = 2.2 \times 10^{42} \left( \frac{\Omega_c}{4\pi} \right) \left( \frac{n_H}{10^8 \text{cm}^{-3}} \right) \left( \frac{R_c}{1 \text{pc}} \right)^2 \left( \frac{\sigma_{\text{abs}}}{100 \text{km s}^{-1}} \right)^3 \text{erg s}^{-1}, \quad (5)$$

which are comparable to the bolometric luminosity of the AGN,  $L_{\text{bol}} \sim 10^{44}$  erg s $^{-1}$ .

The outcome of the previous estimates depends on two very uncertain assumptions. The large-scale covering factor of the dense absorbers, and the turbulence decay time,  $\delta R_c / \sigma_{\text{abs}}$ . Based on the fraction of LRDs with confirmed line absorption, it is reasonable to estimate  $\Omega_c / (4\pi) > 0.1$ , which would imply that the absorbing clouds are an important component of the energy budget in LRD AGN. For the turbulence decay time, we have assumed the smallest physical size of the clouds. However, since the resulting crossing time is only of order 10 yr, it is difficult to imagine these clouds being long lived, which is required to explain the relatively high fraction of LRDs with absorption. It is thus possible that the absorbing gas constitutes the limiting edge of the Strömgren sphere, and that it is therefore contiguous to higher ionization gas, perhaps the BLR itself. In this case, the decay time would be significantly longer, depending on the actual scale of the turbulence. Alternatively, the observed  $\sigma_{\text{abs}}$  may represent a velocity dispersion between different clouds, but in this case we would expect significant cloud-cloud collisions. Still, a dynamical environment, where absorbing clouds are continuously formed and destroyed on short timescales is also possible, and it is supported by observations of gas absorption in local AGN (Maiolino et al. 2010, although, in the latter case, the absorption is much weaker).

#### 4.3 Black hole mass and Eddington accretion rate

Our estimate of  $M_\bullet$  is roughly one order of magnitude lower than previous values based on H $\beta$  (cf. hexagon vs large circle in Fig. 4). Since H $\alpha$  is much brighter and has a much higher SNR than H $\beta$ ,

we favour the current lower estimate. The non-Gaussian profile of the emission line has been observed in normal AGN too, and could indicate radiative transfer effects such as electron scattering in high-density gas (e.g., ?). Depending on which method is used (i.e., *RV15* or *DB25*), our  $M_\bullet$  estimates span the range  $\log(M_\bullet/M_\odot) = 6.3\text{--}6.7$ , (after accounting for a 0.2 dex dust-attenuation correction using the value of  $A_{V,n}$  derived from the Balmer decrement of the narrow lines. These are very low  $M_\bullet$  values; on one hand, they are comparable to the mass of Sgr A\* (*GRAVITY Collaboration et al. 2022; The Event Horizon Telescope Collaboration 2023*) in the local Universe, which is found at the centre of a galaxy 300 times more massive. At the other extreme, the SMBH in Abell2744-QSO1 is comparable to the one in GN-z11, a much more massive galaxy at  $z = 10.6$  (*Oesch et al. 2016; Bunker et al. 2023; Maiolino et al. 2024a*). With the bolometric luminosity estimated from H  $\alpha$  (or, equivalently, from the optical continuum, *J25*), we infer high values of the accretion rate, comparable or even beyond the Eddington limit. Even with relatively short duty cycles, such high accretion rates could explain the rapid growth of black holes in the first billion years after the Big Bang – perhaps even starting from relatively low-mass seeds (*Koudmani et al. 2022; Schneider et al. 2023; Bennett et al. 2024; Trinca et al. 2024; Huško et al. 2025; Koudmani S., in prep.*).

While our lower black hole mass relaxes the discrepancy with dynamical mass, we also revise the width of the narrow lines to lower values than *J25*, which reduces the dynamical mass of the whole system to the range  $\log(M_{\text{dyn}}/M_\odot) = 7.1\text{--}8.0$  (depending on the calibration adopted). With these values, we obtain a range of  $M_\bullet/M_{\text{dyn}}$  between 0.02 and 0.4. A value of 0.02 would be in tension, but possibly still consistent, with the  $M_\bullet\text{--}\sigma$  relation inferred from the narrow lines (*Maiolino et al. 2024b*), supporting the scenario of co-evolution between SMBHs and the baryon mass of their host galaxies (since the effective radius is smaller than  $R_e < 30$  pc, we can ignore dark matter; Section 3.1). On the other hand, a value of 0.4 would indicate a strong deviation not only of the  $M_\bullet\text{--}M_\star$  relation, but even of the  $M_\bullet\text{--}\sigma$  relation, suggesting a departure from the co-evolution path (*J25*), possibly associated with a black hole-first scenario. The largest uncertainty on these ratios derives from the galaxy virial calibrations, which span one dex in  $M_{\text{dyn}}$ . In Fig. 4a we show the  $M_\bullet\text{--}M_\star$  relation, where we use our most conservative upper limit on  $M_{\text{dyn}}$  as an upper limit on  $M_\star$  too; despite revising  $M_\bullet$  down, we confirm that the SMBH in Abell2744-QSO1 makes up at least 2 percent of the stellar mass.

Analysis of black holes evolutionary tracks in scenarios where  $z \sim 5$  over massive black holes grow through short phases of super-Eddington accretion suggest that they tend to grow independently of their final host galaxy (in independent progenitor halos) down to  $z \sim 8$ , and start ‘co-evolving’ only thereafter (*Trinca et al. 2024*). Before that, their BH to stellar mass ratio may be even more extreme than observed at  $z \sim 5$ .

In Fig. 4b we compare our new measurements to local scaling relations between  $M_\bullet$  and  $M_{\text{dyn}}$ , and confirm the overmassive nature of the SMBH in Abell2744-QSO1. For this galaxy to fall near the local relations, we need to adopt simultaneously the lowest estimate on  $M_\bullet$  ( $M_{\bullet,\text{ism}}^{\text{RV15}}$ ) and the highest upper limit on  $M_{\text{dyn}}$ , giving  $M_{\bullet,\text{ism}}^{\text{RV15}}/M_{\text{dyn}} > 0.02$ . Our highest estimate is  $M_{\bullet,\text{ism}}^{\text{DB25}}/M_{\text{dyn}} > 0.4$ , at the same level as what inferred for another LRD, Abell2744-49524, based on a tentative detection of [C I] $\lambda 370\ \mu\text{m}$  (*Akins et al. 2025*). In any case, regardless of the  $M_\bullet$  and  $M_{\text{dyn}}$  adopted, the SMBH is a dominant component of the dynamics of this system, with a sphere of influence of 18–45 pc, which is comparable to or even larger than the upper limit on  $R_e$ .

The observation of turbulent gas absorbers consistent with rest-

frame velocities, together with their low dust (and metallicity, *J25*) content and with high  $\lambda_{\text{Edd}}$  ratios, suggests a scenario where accreted gas is piled up in a dense reservoir near the black hole, giving rise to long-lived absorption (*Fabian et al. 2008*).

While radiation pressure should normally be able to clear this gas, several conditions in the early Universe may favour gas accumulation. Accreting gas at early times would naturally have low angular momentum (since low-angular momentum gas would collapse earlier and more efficiently; e.g., *Renzi et al. 2025*), leading to a high accretion rate towards the innermost regions of proto-galaxies, where massive black holes dominate the gravitational potential. The compact nature of LRDs naturally agrees with a low-angular-momentum budget, and the high black-hole to total mass fraction supports scenarios of black-hole dominated galaxies (*J25*).

While radiation pressure would push the gas outwards, high gas density, metals and dust just outside the sublimation zone would favour gas cooling. At the same time, the very low metallicity and dust content of newly accreted gas mean that its coupling to the accretion-disc radiation is essentially driven by the Thomson cross section, not by dust absorption. This is different from later epochs and from more evolved galaxies, where dust in the ISM increases the coupling with radiation up to ten- or hundred-fold relative to the Thomson cross section (*Fabian et al. 2008*). If this gas is stalling due to weak radiation pressure, it would naturally have a high degree of turbulence, but negligible radial velocity, consistent with observations. Its accumulation would lead to high covering factors, also consistent with observations.

In this scenario, the SMBH would be unable to regulate gas accretion onto the galaxy (*Pacucci & Narayan 2024*), explaining why the  $M_\bullet\text{--}M_\star$  relation does not hold for proto-galaxies at  $z \gtrsim 5$  (*Harikane et al. 2023; Maiolino et al. 2024b*), but why it is in place at lower redshifts and for more massive, more evolved galaxies (*Sun et al. 2025*). Indeed, at later epochs, metal dissemination from the first galaxies and higher angular momentum would lead to larger galaxies, where the impact of the central SMBH on the gravitational potential of the host galaxy becomes negligible (except for the innermost regions), but where its ability to regulate the galaxy ISM increases dramatically. This evolution would naturally explain the disappearance of LRDs at later epochs, which currently seems to occur by  $z \sim 2$  (*Juodžbalis et al. 2024a*).

## 5 CONCLUSIONS

In this work, we present  $R = 3,700$  *JWST* NIRSpec/IFS aperture spectroscopy of the H  $\alpha$  line in the broad-line AGN Abell2744-QSO1 at  $z = 7.04$ . Leveraging the higher SNR of these data, we find

- The H  $\alpha$  emission line consists of a narrow-line component (8- $\sigma$  detection) and a broad-line component. The latter has distinctively non-Gaussian line profile with observed  $FWHM = 560 \pm 70$  km s $^{-1}$ .
- From the Balmer decrement of the narrow lines, we infer  $A_V = 1.4 \pm 0.4$  mag. Interpreting the narrow H  $\alpha$  line as solely due to star formation, we infer a de-lensed SFR of  $2.5_{-0.08}^{+0.12} M_\odot \text{ yr}^{-1}$ .
- Our revised SMBH masses range from  $\log(M_{\bullet,\text{ism}}^{\text{RV15}}/M_\odot) = 6.3$  (*RV15* calibration) to  $\log(M_{\bullet,\text{ism}}^{\text{DB25}}/M_\odot) = 6.7$  (*DB25* calibration).
- Assuming local calibrations for the bolometric AGN luminosity, we infer Eddington ratios  $\lambda_{\text{Edd}} = 0.4\text{--}1.6$ .
- The narrow line has an intrinsic  $\sigma_n = 22_{-6}^{+7}$  km s $^{-1}$ , a measurement we deem reliable based on the high SNR of the line itself (*Zhou et al. 2017*). The resulting  $M_{\text{dyn}}$  is  $\log(M_{\text{dyn}}/M_\odot) = 7.1\text{--}8.0$ , implying very high  $M_\bullet/M_{\text{dyn}} = 0.01\text{--}0.4$ .



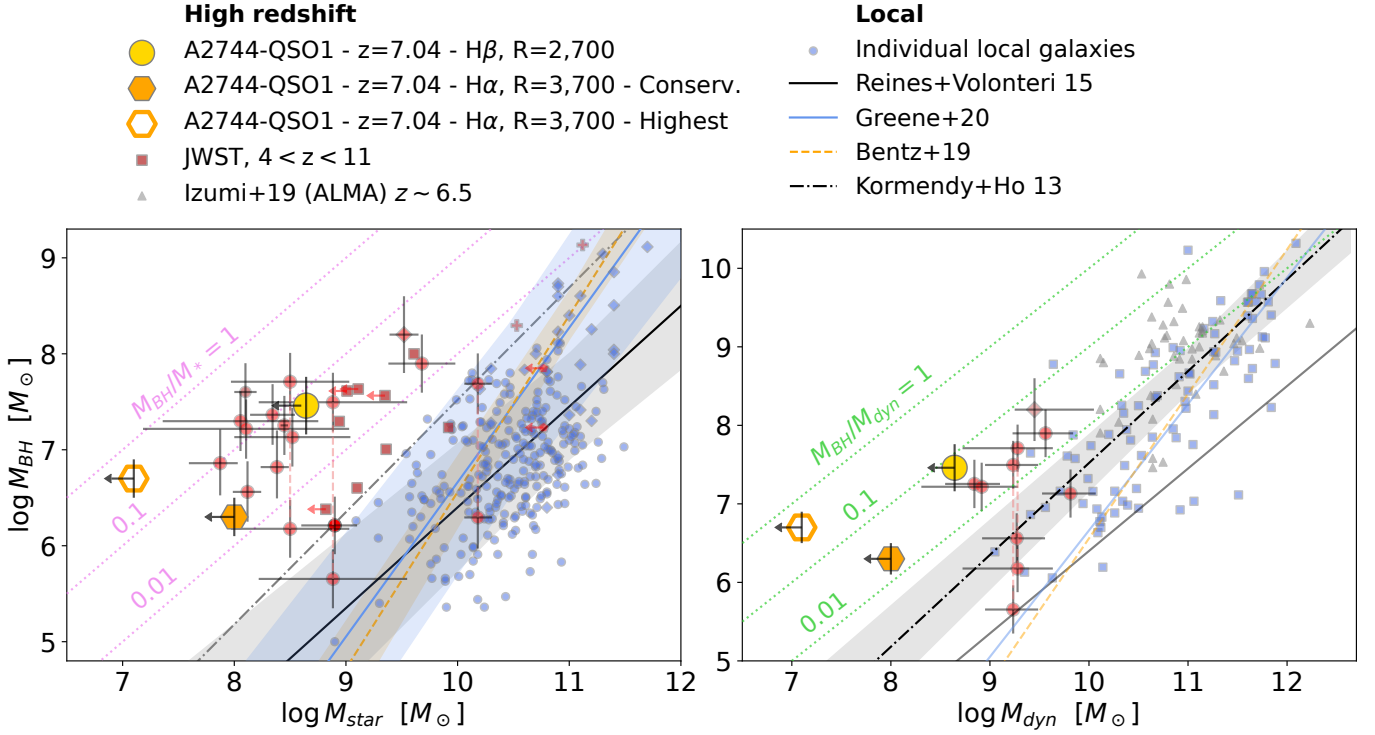


**Figure 4.** Using our fiducial determination of  $M_{\bullet}$ ,  $M_{\bullet}^{\text{DB25}}$ , Abell2744-QSO1 (orange hexagon) is overmassive relative to both  $M_{\star}$  (panel a) and  $M_{\text{dyn}}$  (panel b), when compared to local scaling relations, similar to other JWST-discovered AGN (red symbols). Our estimates based on H $\alpha$  revise both  $M_{\bullet}$  and  $M_{\text{dyn}}$  down relative to the H $\beta$  and [O III] $\lambda$ 5007 estimates (large yellow circle; J25), such that the main conclusions of J25 remain unchanged.

- Broad H $\alpha$  is subject to foreground hydrogen Balmer-line absorption with high EW and large broadening  $\sigma_{\text{abs}} = 100 \pm 10 \text{ km s}^{-1}$ , which rules out a stellar origin. This detection confirms the predictions of Inayoshi & Maiolino (2025) and J25 of a link between AGNs with Balmer breaks and Balmer-line absorption. Our  $\sigma_{\text{abs}}$  is consistent with the micro-turbulence inferred from independent modelling of the Balmer break by J25.

- The H $\alpha$  absorber has the same line-of-sight velocity as the broad H $\alpha$  emission line and is very close to the velocity of the narrow lines, implying that the absorbing gas cannot be interpreted as an inflow or outflow.

- Comparing the column density and ISM attenuation of the galaxy, we infer that the  $n = 2$  absorber is dust poor.

Our findings confirm the overmassive nature of the SMBHs in low-luminosity, ‘LRD’ AGNs. The overmassive nature of Abell2744-QSO1 suggests intriguing possibilities regarding the formation of early SMBHs, such as SMBHs dominating the gravitational potential, and large supply of cosmic gas that can be efficiently fuelled onto SMBHs leading to (super)-Eddington accretion rates.

## DATA AVAILABILITY

This work is based on observations made with the NASA/ESA/CSA James Webb Space Telescope. The data were obtained as part of JWST program ID 5015, and are available from the Mikulski Archive for Space Telescopes at the Space Telescope Science Institute, which is operated by the Association of Universities for Research in Astronomy, Inc., under NASA contract NAS 5-03127 for JWST. The reduced data will be made available after review.

We are grateful to Claudia Di Cesare for sharing the DUSTYGADGET results. FDE, RM, GCJ, XJ, WM and JS acknowledge support by the Science and Technology Facilities Council (STFC), by the ERC through Advanced Grant 695671 ‘‘QUENCH’’, and by the UKRI Frontier Research grant RISEandFALL. RM also acknowledges funding from a research professorship from the Royal Society. GM acknowledges financial support from the grant PRIN MIUR 2017PH3WAT (‘Black hole winds and the baryon life cycle of galaxies’). SC and GV acknowledge support by European Union’s HE ERC Starting Grant No. 101040227 - WINGS. MVM is supported by the National Science Foundation via AAG grant 2205519, the Wisconsin Alumni Research Foundation via grant MSN251397, and NASA via STScI grant JWST-GO-4426. AJB acknowledges funding from the ‘‘FirstGalaxies’’ Advanced Grant from the European Research Council (ERC) under the European Union’s Horizon 2020 research and innovation program (Grant agreement No. 789056). ST acknowledges support by the Royal Society Research Grant G125142. CT acknowledges support from STFC grants ST/R000964/1 and ST/V000853/1. H $\ddot{U}$  acknowledges funding by the European Union (ERC APEX, 101164796). Views and opinions expressed are however those of the authors only and do not necessarily reflect those of the European Union or the European Research Council Executive Agency. Neither the European Union nor the granting authority can be held responsible for them. MP acknowledges grant PID2021-127718NB-I00 funded by the Spanish Ministry of Science and Innovation/State Agency of Research (MICIN/AEI/ 10.13039/501100011033), and the grant RYC2023-044853-I, funded by MICIU/AEI/10.13039/501100011033 and European Social Fund Plus (FSE+).

This work made extensive use of the freely available Debian

GNU/Linux operating system. We used the Python programming language (van Rossum 1995), maintained and distributed by the Python Software Foundation. We made direct use of Python packages `ASTROPY` (Astropy Collaboration et al. 2013), `CORNER` (Foreman-Mackey 2016), `EMCEE` (Foreman-Mackey et al. 2013), `JWST` (Alves de Oliveira et al. 2018), `MATPLOTLIB` (Hunter 2007), `NUMPY` (Harris et al. 2020), and `SCIPY` (Jones et al. 2001). We also used the software `TOPCAT`, (Taylor 2005), `FITSMAP` (Hausen & Robertson 2022), and `DS9` (Joye & Mandel 2003).

## AFFILIATIONS

<sup>11</sup>*Sorbonne Université, CNRS, UMR 7095, Institut d'Astrophysique de Paris, 98 bis bd Arago, 75014 Paris, France*

<sup>12</sup>*INAF - Osservatorio Astrofisico di Arcetri, largo E. Fermi 5, 50127 Firenze, Italy*

<sup>13</sup>*Dipartimento di Fisica e Astronomia "G. Galilei", Università di Padova, Vicolo dell'Osservatorio 3, I-35122 Padova, Italy*

<sup>14</sup>*INAF - Osservatorio Astronomico di Padova, Vicolo dell'Osservatorio 5, I-35122 Padova, Italy*

<sup>15</sup>*Jeremiah Horrocks Institute, University of Central Lancashire, Preston, PR1 2HE, UK*

<sup>16</sup>*Steward Observatory, University of Arizona, 933 N. Cherry Ave., Tucson, AZ, 85721, USA*

<sup>17</sup>*Dipartimento di Fisica e Astronomia, Università di Firenze, Via G. Sansone 1, I-50019, Sesto F.no (Firenze), Italy*

<sup>18</sup>*Dipartimento di Fisica e Astronomia, Università di Bologna, Via Gobetti 93/2, I-40129 Bologna, Italy*

<sup>19</sup>*INAF - Osservatorio di Astrofisica e Scienza dello Spazio di Bologna, Via Gobetti 93/3, I-40129 Bologna, Italy*

<sup>20</sup>*Department for Astrophysical and Planetary Science, University of Colorado, Boulder, CO 80309, USA*

<sup>21</sup>*Department of Astronomy and Astrophysics, University of California, Santa Cruz, Santa Cruz, CA 95064 USA*

<sup>22</sup>*Dipartimento di Fisica, Sapienza Università di Roma, Piazzale Aldo Moro 2, 00185 Roma, Italy*

<sup>23</sup>*NRC Herzberg, 5071 West Saanich Rd, Victoria, BC V9E 2E7, Canada*

<sup>24</sup>*Cosmic Dawn Center (DAWN), Copenhagen, Denmark*

<sup>25</sup>*Niels Bohr Institute, University of Copenhagen, Jagtvej 128, DK-2200, Copenhagen, Denmark*

<sup>26</sup>*Department of Astronomy, University of Geneva, Chemin Pegasi 51, 1290 Versoix, Switzerland*

## REFERENCES

Akins H. B., et al., 2025, *arXiv e-prints*, p. [arXiv:2503.00998](https://arxiv.org/abs/2503.00998)

Alves de Oliveira C., et al., 2018, in *Observatory Operations: Strategies, Processes, and Systems VII*. p. 107040Q ([arXiv:1805.06922](https://arxiv.org/abs/1805.06922)), doi:[10.1117/12.2313839](https://doi.org/10.1117/12.2313839)

Arakawa N., Fabian A. C., Ferland G. J., Ishibashi W., 2022, *MNRAS*, **517**, 5069

Arellano-Córdova K. Z., Esteban C., García-Rojas J., Méndez-Delgado J. E., 2021, *MNRAS*, **502**, 225

Astropy Collaboration et al., 2013, *A&A*, **558**, A33

Baggen J. F. W., et al., 2024, *ApJ*, **977**, L13

Barat D., et al., 2019, *MNRAS*, **487**, 2924

Bechtold K., Böker T., Franz D. E., te Plate M., Rawle T. D., Wu R., Zeidler P., 2024, *arXiv e-prints*, p. [arXiv:2408.15940](https://arxiv.org/abs/2408.15940)

Begelman M. C., Volonteri M., Rees M. J., 2006, *MNRAS*, **370**, 289

Bennett J. S., Sijacki D., Costa T., Laporte N., Witten C., 2024, *MNRAS*, **527**, 1033

Bezanson R., et al., 2018, *ApJ*, **868**, L36

Böker T., et al., 2022, *A&A*, **661**, A82

Bromm V., Loeb A., 2003, *Nature*, **425**, 812

Bullock J. S., Kolatt T. S., Sigad Y., Somerville R. S., Kravtsov A. V., Klypin A. A., Primack J. R., Dekel A., 2001, *MNRAS*, **321**, 559

Bunker A. J., et al., 2023, *A&A*, **677**, A88

Carnall A. C., et al., 2023, *Nature*, **619**, 716

Chabrier G., 2003, *PASP*, **115**, 763

Choi J., Dotter A., Conroy C., Cantiello M., Paxton B., Johnson B. D., 2016, *ApJ*, **823**, 102

Conroy C., Naidu R. P., Zaritsky D., Bonaca A., Cargile P., Johnson B. D., Caldwell N., 2019, *ApJ*, **887**, 237

Cortese L., et al., 2016, *MNRAS*, **463**, 170

D'Eugenio F., et al., 2024, *A&A*, **689**, A152

Dalla Bontà E., et al., 2024, *arXiv e-prints*, p. [arXiv:2410.21387](https://arxiv.org/abs/2410.21387)

Di Cesare C., Graziani L., Schneider R., Ginolfi M., Venditti A., Santini P., Hunt L. K., 2023, *MNRAS*, **519**, 4632

Dojčinović I., Kovačević-Dojčinović J., Popović L. Č., 2023, *Advances in Space Research*, **71**, 1219

Dong X., Wang T., Wang J., Yuan W., Zhou H., Dai H., Zhang K., 2008, *MNRAS*, **383**, 581

Dubois Y., Volonteri M., Silk J., Devriendt J., Slyz A., Teyssier R., 2015, *MNRAS*, **452**, 1502

Dutton A. A., Macciò A. V., 2014, *MNRAS*, **441**, 3359

Eisenstein D. J., et al., 2023, *arXiv e-prints*, p. [arXiv:2306.02465](https://arxiv.org/abs/2306.02465)

Fabian A. C., 2012, *ARA&A*, **50**, 455

Fabian A. C., Vasudevan R. V., Gandhi P., 2008, *MNRAS*, **385**, L43

Ferrarese L., Merritt D., 2000, *ApJ*, **539**, L9

Ferruit P., et al., 2022, *A&A*, **661**, A81

Fiore F., et al., 2017, *A&A*, **601**, A143

Foreman-Mackey D., 2016, *The Journal of Open Source Software*, **1**, 24

Foreman-Mackey D., Hogg D. W., Lang D., Goodman J., 2013, *PASP*, **125**, 306

Furtak L. J., et al., 2023, *ApJ*, **952**, 142

Furtak L. J., et al., 2024, *Nature*, **628**, 57

Furtak L. J., et al., 2025, *arXiv e-prints*, p. [arXiv:2502.07875](https://arxiv.org/abs/2502.07875)

GRAVITY Collaboration et al., 2022, *A&A*, **657**, L12

Gebhardt K., et al., 2000, *ApJ*, **539**, L13

Gordon K. D., Clayton G. C., Misselt K. A., Landolt A. U., Wolff M. J., 2003, *ApJ*, **594**, 279

Graziani L., Schneider R., Ginolfi M., Hunt L. K., Maio U., Glatzle M., Ciardi B., 2020, *MNRAS*, **494**, 1071

Greene J. E., et al., 2024, *ApJ*, **964**, 39

Hainline K. N., et al., 2024, *ApJ*, **964**, 71

Harikane Y., et al., 2023, *ApJ*, **959**, 39

Harris C. R., et al., 2020, *Nature*, **585**, 357

Hausen R., Robertson B. E., 2022, *Astronomy and Computing*, **39**, 100586

Henden N. A., Puchwein E., Shen S., Sijacki D., 2018, *MNRAS*, **479**, 5385

Hunter J. D., 2007, *Computing in Science and Engineering*, **9**, 90

Huško F., Lacey C. G., Roper W. J., Schaye J., Briggs J. M., Schaller M., 2025, *MNRAS*, **537**, 2559

Ilić D., Popović L. Č., La Mura G., Ciroi S., Rafanelli P., 2012, *A&A*, **543**, A142

Inayoshi K., Maiolino R., 2025, *ApJ*, **980**, L27

Inayoshi K., Visbal E., Haiman Z., 2020, *ARA&A*, **58**, 27

Jakobsen P., et al., 2022, *A&A*, **661**, A80

Ji X., et al., 2025, *arXiv e-prints*, p. [arXiv:2501.13082](https://arxiv.org/abs/2501.13082)

Jones E., Oliphant T., Peterson P., et al., 2001, *SciPy: Open source scientific tools for Python*, <http://www.scipy.org/>

Joye W. A., Mandel E., 2003, in Payne H. E., Jedrzejewski R. I., Hook R. N., eds, *Astronomical Society of the Pacific Conference Series Vol. 295, Astronomical Data Analysis Software and Systems XII*. p. 489

Juodžbalis I., et al., 2024a, *MNRAS*, **535**, 853

Juodžbalis I., et al., 2024b, *Nature*, **636**, 594

Kannan R., et al., 2025, *arXiv e-prints*, p. [arXiv:2502.20437](https://arxiv.org/abs/2502.20437)

Kocevski D. D., et al., 2023, *ApJ*, **954**, L4

Kokorev V., et al., 2023, *ApJ*, **957**, L7

Kokubo M., Harikane Y., 2024, *arXiv e-prints*, p. [arXiv:2407.04777](https://arxiv.org/abs/2407.04777)

Konstantopoulou C., et al., 2024, *A&A*, 681, A64  
 Kormendy J., Ho L. C., 2013, *ARA&A*, 51, 511  
 Koudmani S., Sijacki D., Smith M. C., 2022, *MNRAS*, 516, 2112  
 Labbe I., et al., 2025, *ApJ*, 978, 92  
 Latif M. A., Ferrara A., 2016, *Publ. Astron. Soc. Australia*, 33, e051  
 Li J., Shen Y., Zhuang M.-Y., 2025, arXiv e-prints, p. arXiv:2502.05048  
 Ma Y., et al., 2024, arXiv e-prints, p. arXiv:2410.06257  
 Maiolino R., et al., 2010, *A&A*, 517, A47  
 Maiolino R., et al., 2024a, *Nature*, 627, 59  
 Maiolino R., et al., 2024b, *A&A*, 691, A145  
 Marconi A., Hunt L. K., 2003, *ApJ*, 589, L21  
 Matthee J., et al., 2024, *ApJ*, 963, 129  
 McClymont W., et al., 2025, arXiv e-prints, p. arXiv:2503.00106  
 McConnell N. J., Ma C.-P., 2013, *ApJ*, 764, 184  
 Moseley S. H., Arendt R. G., Fixsen D. J., Lindler D., Loose M., Rauscher B. J., 2010, in Holland A. D., Dorn D. A., eds, Society of Photo-Optical Instrumentation Engineers (SPIE) Conference Series Vol. 7742, High Energy, Optical, and Infrared Detectors for Astronomy IV. p. 77421B, doi:10.1117/12.866773  
 Oesch P. A., et al., 2016, *ApJ*, 819, 129  
 Pacucci F., Narayan R., 2024, *ApJ*, 976, 96  
 Perna M., et al., 2023, *A&A*, 679, A89  
 Peterson B. M., et al., 2004, *ApJ*, 613, 682  
 Planck Collaboration et al., 2020, *A&A*, 641, A6  
 Portegies Zwart S. F., Makino J., McMillan S. L. W., Hut P., 1999, *A&A*, 348, 117  
 Rauscher B. J., et al., 2012, in Holland A. D., Beletic J. W., eds, Society of Photo-Optical Instrumentation Engineers (SPIE) Conference Series Vol. 8453, High Energy, Optical, and Infrared Detectors for Astronomy V. p. 84531F, doi:10.1117/12.926089  
 Rauscher B. J., et al., 2017, *PASP*, 129, 105003  
 Rees M. J., 1984, *ARA&A*, 22, 471  
 Reines A. E., Volonteri M., 2015, *ApJ*, 813, 82  
 Renzini A., 2025, *MNRAS*, 536, L8  
 Rieke M. J., et al., 2023, *ApJS*, 269, 16  
 Saglia R. P., et al., 2016, *ApJ*, 818, 47  
 Schneider R., Valiante R., Trinca A., Graziani L., Volonteri M., Maiolino R., 2023, *MNRAS*, 526, 3250  
 Shapley A. E., Sanders R. L., Reddy N. A., Topping M. W., Brammer G. B., 2023, *ApJ*, 954, 157  
 Silk J., 2017, *ApJ*, 839, L13  
 Simmonds C., et al., 2024, *MNRAS*, 535, 2998  
 Smith K. C., Howarth I. D., 1998, *MNRAS*, 299, 1146  
 Stern J., Laor A., 2012, *MNRAS*, 423, 600  
 Storey P. J., Zeppen C. J., 2000, *MNRAS*, 312, 813  
 Stott J. P., et al., 2016, *MNRAS*, 457, 1888  
 Sun Y., et al., 2025, *ApJ*, 978, 98  
 Taylor M. B., 2005, in Shopbell P., Britton M., Ebert R., eds, Astronomical Society of the Pacific Conference Series Vol. 347, Astronomical Data Analysis Software and Systems XIV. p. 29  
 Taylor A. J., et al., 2024, arXiv e-prints, p. arXiv:2409.06772  
 The Event Horizon Telescope Collaboration 2023, arXiv e-prints, p. arXiv:2311.08680  
 Trebitsch M., Volonteri M., Dubois Y., Madau P., 2018, *MNRAS*, 478, 5607  
 Trinca A., et al., 2024, arXiv e-prints, p. arXiv:2412.14248  
 Übler H., et al., 2023, *A&A*, 677, A145  
 Veilleux S., Cecil G., Bland-Hawthorn J., 2005, *ARA&A*, 43, 769  
 Veilleux S., Maiolino R., Bolatto A. D., Aalto S., 2020, *A&ARv*, 28, 2  
 Wang B., et al., 2024a, arXiv e-prints, p. arXiv:2403.02304  
 Wang B., et al., 2024b, *ApJ*, 969, L13  
 Zhou L., et al., 2017, *MNRAS*, 470, 4573  
 Zhu H., Tian W., Li A., Zhang M., 2017, *MNRAS*, 471, 3494  
 van Rossum G., 1995, CWI Technical Report, CS-R9526  
 van der Wel A., et al., 2022, *ApJ*, 936, 9

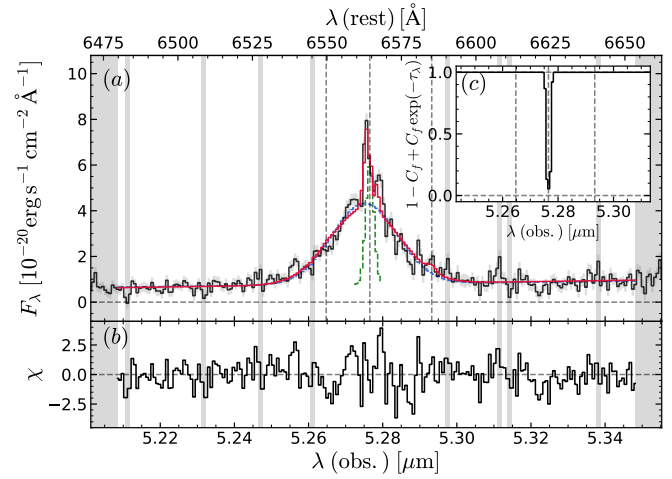


**Figure A1.** Best-fit model of  $H\alpha$  using a single-Gaussian profile for the broad emission. A single Gaussian does not appear to correctly reproduce the line shape, yielding a higher reduced  $\chi^2$  relative to the fiducial model. The panels and line colours are the same as in Fig. 1.

## APPENDIX A: ALTERNATIVE MODELS OF THE BROAD $H\alpha$

The double-Gaussian assumption represents a convenient and effective way to capture the observed shape of the  $H\alpha$  emission. However, in principle, other line shapes are possible, such as a broken power law or a Lorentzian profile. Here we test two alternative approaches; a single Gaussian, and a Voigt profile. The maximum-likelihood single-Gaussian model is shown in Fig. A1. This model yields a worse fit than the fiducial model. For comparison, we calculate the reduced  $\chi^2$  in the spectral window  $5.24 \leq \lambda \leq 5.32 \mu\text{m}$ , and find a reduced  $\chi^2$  of 3.3, compared to 1.9 for the fiducial model. The model presents clear excess blueward and redward of the narrow-line  $H\alpha$ , which in the fiducial fit is attributed to the narrowest of the two broad Gaussians (cf. Fig. 1c). To capture some of this flux, the model uses a broader and redshifted narrow-line, coupled with very strong and very narrow absorption. This is an unfavourable combination, because the redshift of the narrow  $H\alpha$  does not agree with the redshift of  $H\beta$  and  $[\text{O III}]\lambda 5007$ . As a result, the latter two lines, which have lower SNR than narrow  $H\alpha$ , are both clipped as outliers. Furthermore, the extremely narrow absorber (having  $\sigma_{\text{abs}} < 20 \text{ km s}^{-1}$ ,  $3\text{-}\sigma$  upper limit; panel c) is completely inconsistent with the shape of the Balmer break, which is remarkably smooth (Furtak et al. 2024; Ma et al. 2024; J25). More subtle, but still noticeable, is the excess flux around 5.27 and 5.29  $\mu\text{m}$ , also evident as several consecutive pixels with  $\chi < -2$  around these wavelengths in panel b. Nevertheless, the FWHM of this model is still in disagreement with the results found for  $H\beta$ , with the single-Gaussian BLR having  $FWHM_b(H\alpha) = 1190^{+50}_{-50} \text{ km s}^{-1}$ . Hence we reject a single broad-line Gaussian with an absorber as a viable model for the BLR in Abell2744-QSO1.

Next we consider a Voigt profile, which is a more general model than a Lorentzian profile, because the latter reduces to a Voigt profile in the presence of kinematic broadening in the line core. For the case in hand, we have a minimum core broadening of  $\sigma = 34 \text{ km s}^{-1}$  due to the spectral resolution of NIRSpect. Similarly to the single-Gaussian, the Voigt model fails to reproduce the spectral region near narrow  $H\alpha$  (Fig. A2a), leaving strong negative (positive) residuals blueward (redward) of the narrow line (panel b). Using the same

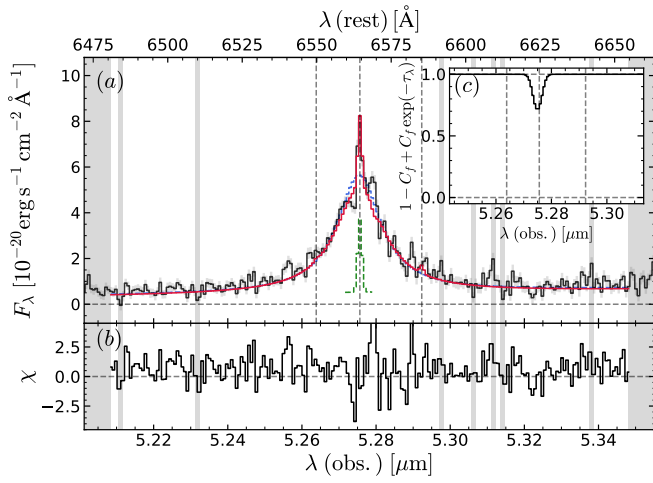


**Figure A2.** Best-fit model of H  $\alpha$  using a Voigt profile for the broad emission. The Voigt (and Lorentzian) profiles do not appear to correctly reproduce the line shape, yielding a higher reduced  $\chi^2$  relative to the fiducial model. The panels and line colours are the same as in Fig. 1.

spectral window as for the single-Gaussian test, we find a reduced  $\chi^2$  value of 3.4, favouring the double-Gaussian model.

This paper has been typeset from a  $\text{\TeX}/\text{\LaTeX}$  file prepared by the author.